J. Fluid Mech. (1999), *vol.* 383, *pp.* 1–28. Printed in the United Kingdom

High-velocity flow in a rough fracture

By E. SKJETNE[1]†, A. HANSEN[2] AND J. S. GUDMUNDSSON[1]

[1]Department of Petroleum Engineering and Applied Geophysics, Norwegian University of Science and Technology, N-7034 Trondheim, Norway

[2]Department of Physics, Norwegian University of Science and Technology, N-7034 Trondheim, Norway

(Received 18 April 1996 and in revised form 27 April 1998)

We simulate high-velocity flow in a self-affine channel with a constant perpendicular opening by solving numerically the Navier–Stokes equations, and analyse the resulting flow qualitatively and quantitatively. At low velocity, i.e. vanishing inertia, the effective permeability is dominated by the narrowest constrictions measured perpendicular to the local flow direction and the flow field tends to fill the channel due to the diffusion generated by the viscous term in the Stokes equation. At high velocity (strong inertia), the high-velocity zones of the flow field resemble a narrow tube of essentially constant thickness in the direction of flow, since the transversal diffusion is weak compared to the longitudinal convection. The thickness of the flow tube decreases with Reynolds number. This narrowing in combination with mass balance results in an average velocity in the flow tube which increases faster with Reynolds number than the average velocity in the fracture. In the low-velocity zones, recirculation zones appear and the pressure is almost constant.

The flow tube consists of straight sections. This is due to inertia. The local curvature of the main stream reflects the flow-tube/channel-wall interaction. A boundary layer is formed where the curvature is large. This boundary layer is highly dissipative and governs the large pressure loss (inertial resistance) of the medium. Quantitatively, vanishing, weak and strong inertial flow regimes can be described by the Darcy, weak inertia and Forchheimer flow equations, respectively. We observe a cross-over flow regime from the weak to strong inertia, which extends over a relatively large range of Reynolds numbers.

1. Introduction

Flow through fracture systems is in many oil reservoirs the dominating fluid transport mechanism. In order to describe such flow, three aspects of the problem must be addressed: (i) a description of the topology of the fracture network, (ii) the geometry of the fracture, and (iii) the flow field within the fracture. The topology of the fracture network reflects the geological history of the reservoir, and has to be addressed in this context (Aviles, Scholz & Boatwright 1987; Hirata 1989; Bour 1991; Velde *et al.* 1991; Vignes-Adler, Le Page & Adler 1991; Davy, Sornette & Sornette 1992; Davy 1993). Calculations of the permeability of such fracture networks based on their topology are reported in e.g. Snow (1969), Rottmann (1984), Balberg (1986), Hestir & Long (1990), Thompson (1991), Odling (1992). The geometry of the fracture

† Present address: Åsgard PETEK, Statoil, N-4035 Stavanger, Norway.

joints is determined by the fracture mechanisms involved. Recent research on these mechanisms has shown that the resulting fracture joint geometries possess statistical scaling properties which transcend the precise mechanisms that produced them: they are self affine (see e.g. Mandelbrot, Passoja & Paullay 1984; Brown & Scholz 1985; Mecholsky, Passoja & Feinberg-Ringel 1989; Bouchaud, Lapassat & Planès 1990; Dauskardt, Haubensak & Richtie 1990; Hansen, Hinrichsen & Roux 1991; Tzschichholz & Pfuff 1991; Måløy *et al.* 1992; Bouchaud 1997; Issa, Hammad & Chudnovsky 1992; Milman *et al.* 1993; Schmittbuhl, Sentier & Roux 1993; Kertész, Horvàth & Weber 1993; Engøy *et al.* 1994; Roux 1994; Abraham *et al.* 1994; Plouraboué *et al.* 1995; Sharon, Gross & Fineberg 1995).

We address in this paper the third aspect of the problem: what are the features of the flow field within the fracture? This question is strongly influenced by the geometry of the fracture joints, and consequently their self-affine character reflects on the scaling properties of the flow field (Roux *et al.* 1993). Numerical studies using lattice gas automata demonstrate that for both low- and high-velocity flow in a two-dimensional self-affine channel with a symmetry axis parallel to the average flow direction, the velocity-dependent permeability (later called effective permeability; (4.12)) is dominated by the area surrounding the narrowest constriction of the channel (Gutfraind & Hansen 1995; Gutfraind, Ippolito & Hansen 1995). This situation is presumably peculiar to two dimensions. In three-dimensional crack geometries (i.e. a two-dimensional fracture surface in a three-dimensional body), we expect this situation to be quite different: narrow constrictions have less importance as the flow simply passes around them.

The flow regimes observed in porous media can be summarized as follows: vanishing inertia described by Darcy's law, weak inertia described by a third-order correction term (Mei & Auriault 1991; Wodie & Levy 1991), and strong inertia described by the Forchheimer equation (Forchheimer 1901). The Darcy law has been supported experimentally, numerically and theoretically. The same strong support is not found for the two other equations. The weak inertia equation has some numerical support. Barrère (1990) observed the third-order term for Reynolds numbers to be larger than unity, whereas the theory is based on the assumption that the Reynolds number is much smaller than unity. Recently, Skjetne (1995) found that the weak inertia equation is valid for low Reynolds number flow through a close cubic packing of spheres and other periodic porous media. Experimentally, a weak inertia flow regime is supported by the early data referred to by Muskat (1937) and also from the experiments by Chauveteau (1965) and Rasoloarijaona & Auriault (1994). The Forchheimer equation is an empirical equation that has been applied for almost 100 years in porous media research, but still lacks analytical support. This is probably due to a combination of the complexity of the governing equations (the Navier–Stokes equations) and the geometry of natural porous media. There have been several numerical studies of high-velocity flow in porous media (Couland, Morel & Caltagirone 1988; Edwards *et al.* 1990; Barrère 1990; Gipouloux 1992; Souto 1993; Ruth & Ma 1993). Skjetne (1995) studied the microscopic dissipative mechanisms that contribute to the increase in pressure loss in the weak inertia and the Forchheimer equations for flow in porous media.

We study in this paper both low- and high-velocity flow in a two-dimensional self-affine fracture in the light of the three flow regimes found in porous media. This is possible as one might view the fracture as a pore with a particular geometry in a porous medium. As we shall see, this identification gives us access to results already obtained for porous media. In contrast to Gutfraind & Hansen (1995) and Gutfraind

et al. (1995), our self-affine fracture has a constant opening, i.e. we are studying fracture *joints* in contrast to fracture *faults*. The cited papers used channels that were symmetric about an axis parallel to the average flow direction. Our numerical approach is based on a finite-difference discretization of the Navier–Stokes equations.

The paper is organized as follows. In § 2 we describe the geometry of the fracture on different scales. The flow problem is introduces in § 3. Various forms of macroscopic flow equations are presented in § 4. The numerical technique is briefly described in § 5. Results for the microscopical flow are described, analysed and discussed in § 6 and average flow properties are compared to macroscopic flow equations in § 7. How inertial effects lead to increased viscous resistance is discussed in particular in § 8. Finally, the conclusions are listed in § 9.

2. Geometry of the fracture

2.1. *Self-affine fracture*

As was pointed out in the introduction, there is now ample evidence, both experimental and numerical, that fracture surfaces are self-affine. We therefore model the micro geometry of a natural fracture by a cell containing a two-dimensional statistically self-affine fracture with a constant opening perpendicular to the fracture orientation. We choose to study fracture *joints,* i.e. cracks with constant opening resulting from mode I fracturing (Lawn 1993), rather than faults. Joints are common in a geological context. Our conditions apply to the middle sections of mode I fractures. Near the fracture tips, the fracture opening is wedge shaped.

A self-affine roughness profile $y(x)$ is statistically invariant under an affine transformation of a parallel distance d_x and a perpendicular distance d_y

$$d_x \to \lambda_x d_x, \tag{2.1}$$

$$d_y \to \lambda_y d_y, \tag{2.2}$$

where

$$\lambda_y = \lambda_x^H. \tag{2.3}$$

H is the Hurst or roughness exponent (Mandelbrot 1982; Barabási & Stanley 1995). In particular, this leads to the height–height correlation function $p(y_2 - y_1, x_2 - x_1)$ being invariant under the scaling

$$\lambda^H p(\lambda^H (y_2 - y_1), \lambda (x_2 - x_1)) = p(y_2 - y_1, x_2 - x_1)\,. \tag{2.4}$$

Experimentally, $H \approx 0.8$ for two-dimensional fractures in three-dimensional bodies (see e.g. Bouchaud *et al.* 1990; Måløy *et al.* 1992), while $H \approx 0.7$ in two dimensions (Hansen *et al.* 1991; Kertész *et al.* 1993; Engøy *et al.* 1994). These values seem remarkably constant from material to material, and it has been speculated that the roughness exponent is in fact strictly equal in all cases. These ideas have their origin in the theory of dynamical critical phenomena, see e.g. Barabási & Stanley (1995).

A full description of a self-affine surface will need the lower cutoff – discretization – in the x-direction, ϵ, the lower cutoff in the y-direction, η, the length of the fracture in the x-direction, L_u, and the width of the fracture in the y-direction, W. The relation between all of these variables is

$$W = \eta \left(\frac{L_u}{\epsilon} \right)^H. \tag{2.5}$$

The roughness amplitude is thus η/ϵ^H. In addition to these variables describing the

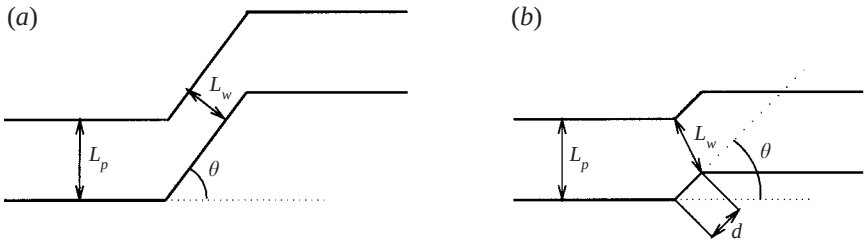

FIGURE 1. The effective channel width for different configurations: (*a*) long-sloped channel, and (*b*) short-sloped channel.

surface, we also have the fracture aperture – the vertical displacement of the two opposite fracture surfaces – L_p as a parameter.

Usually, self-affine geometries are studied for their scaling properties. However, we use such a geometry in order to study the local mechanisms of high-velocity flow in a simplified geometry, but still including a realistic disorder.

If one fixes the fracture opening L_p, the roughness of the fracture W will eventually dominate L_p at large enough scales L_u. This is irrelevant in our context, however. The effect of roughness on the flow field is to force it to change direction and speed. This happens on scales where the roughness is of the same order as L_p. Roughness on larger scales does not contribute. On the other other hand, on scales where L_p is much larger than the roughness W, the flow field is only affected near the boundaries.

We discretize the unit cell into $N \times M$ square cells, in the directions parallel (x) and perpendicular (y) to the fracture average direction, respectively. Each cell is of size $(\Delta x)(\Delta y)$, and the cells are square $\Delta x = \Delta y$. The discrete distances in the parallel and perpendicular directions are

$$x_n = n\,\Delta x, \quad n \in 0,\ldots,N; \quad y_m = m\,\Delta y, \quad m \in 0,\ldots,M. \tag{2.6}$$

In this study we have used $N = 256$, $M = 61$, and a perpendicular fracture opening

$$L_p = 20\,\Delta x. \tag{2.7}$$

Self-affine roughness profiles can be generated by several methods (Voss 1985). We have chosen to use the Fourier method, since this method automatically results in a profile with the desired periodicity. We have chosen $H = 0.8$ in order to mimic real fractures. The resulting roughness profile is discretized in the y-direction to obtain a 256×61 grid.

2.2. *Effective fracture width*

A local effective width of the fracture $L_w(x)$, can be defined as the constriction measured perpendicular to the local flow direction. Since the pressure drop is strongly dependent on L_w, we discuss it in some detail. For a straight fracture, $L_w = L_p$. For a slope with an angle θ defined in figure 1(*a*),

$$L_w = L_p \cos(\theta). \tag{2.8}$$

A linear piece with a smaller length d, such that $d < L_p \sin(\theta)$, L_w can be one of the diagonals of a parallelogram, where the shortest is shown in figure 1(*b*):

$$L_w = \left[L_p^2 + d^2 \pm 2L_p d|\sin\theta|\right]^{1/2}. \tag{2.9}$$

Rough fractures need a further distinction of geometrical features.

A solid filled wedge pointing into the fracture will be called a tooth, while its inverted counterpart on the vertically opposite part of the fracture will be called a trough. These features are always introduced as opposite tooth/trough pairs. Analogous to L_w in figure 1(*b*), L_w of a rough profile can be given by the distance between two diagonally opposing teeth, as can be seen at the constriction at $x = 44\,\Delta x$ in figure 2(*a*), § 6. With reference to the position on one profile, two diagonally opposite teeth are always a pair consisting of one tooth on the profile and a nearest neighbour trough.

2.3. *Large-scale structure of the system*

Our model consists of an infinite two-dimensional spatially periodic structure with repeated unit cells of size L_u. These unit cells consists of a solid matrix in which there is a self-affine fracture with an opening of size L_p. The position vector relative to an origin O is $\boldsymbol{R}$ and can be decomposed into one vector for the position of the unit cell $\boldsymbol{R}_{\boldsymbol{k}}$, where $\boldsymbol{k}$ is the cell-index vector, and the local position inside the unit cell $\boldsymbol{r}$, and is given by

$$\boldsymbol{R} = \boldsymbol{R}_{\boldsymbol{k}} + \boldsymbol{r} \tag{2.10}$$

The fluid and solid volumes sum to the total volume (area in two dimensions) of a unit cell

$$\tau_0 = \tau_f + \tau_s. \tag{2.11}$$

It is convenient to define a porosity

$$\phi = \frac{\tau_f}{\tau_0}, \tag{2.12}$$

in order to make a connection to work done on high-velocity flow in porous media. Our model has a porosity given by the ratio of fluid to solid cells, that is $\phi = 0.328$. The fluid–solid interface is denoted by $\partial\tau_{fs}$.

3. Flow problem

The flow problem is governed by the steady-state Navier–Stokes equations for an incompressible (no-slip) fluid

$$\nabla \cdot \boldsymbol{u} = 0, \tag{3.1}$$

$$-\nabla p = -\mu\nabla^2\boldsymbol{u} + \rho\nabla \cdot (\boldsymbol{uu}), \tag{3.2}$$

$$\boldsymbol{u} = \boldsymbol{0} \quad \text{at} \quad \partial\tau_{fs}, \tag{3.3}$$

where p is the pressure, $\boldsymbol{u}$ is the local velocity vector, μ is the viscosity and ρ is the density. The Reynolds number Re is a rough estimate of the ratio of inertial to viscous forces, and for a characteristic velocity u and length scale L_p is

$$Re = \frac{\rho u L_p}{\mu}. \tag{3.4}$$

As the viscous term in (3.2) is a diffusion term, the Reynolds number can be interpreted as the ratio of the velocity of convection u to the velocity of diffusion $\mu/(\rho L_p)$ of the velocity field itself. The diffusion constant for the velocity field is then μ/ρ.

The large-scale structure of the flow problem is, as noted earlier, conveniently described in terms of spatially periodic porous media, since the fracture is modelled as a spatially periodic structure. General properties of transport in spatially periodic

porous media can be found in Adler (1992). The average of (3.1) over τ_0 is obtained by using the Gauss theorem and the no-slip boundary condition (3.3)

$$\frac{1}{\tau_0}\int_{\tau_0} \nabla \cdot \boldsymbol{u} \mathrm{d}^3\boldsymbol{r} = \frac{1}{\tau_0}\int_{\partial\tau_0} \boldsymbol{u} \cdot \mathrm{d}\boldsymbol{s} = 0, \tag{3.5}$$

where $\boldsymbol{s}$ is the area directed out of the unit cell.

Average mass balance can be satisfied in general only if $\boldsymbol{u}$ is spatially periodic. A spatial average of the velocity is the seepage or Darcy velocity

$$\overline{\boldsymbol{u}} = \frac{1}{\tau_0}\int_{\tau_0} \boldsymbol{u} \mathrm{d}^3\boldsymbol{r}, \tag{3.6}$$

and the velocity averaged over the fluid volume τ_f is the so-called interstitial velocity $\boldsymbol{u}^*$

$$\boldsymbol{u}^* = \frac{1}{\tau_f}\int_{\tau_0} \boldsymbol{u} \mathrm{d}^3\boldsymbol{r} = \frac{\overline{\boldsymbol{u}}}{\phi}. \tag{3.7}$$

In our case, the porosity is artificial. The interstitial velocity is relevant for describing the flow. However, we will use the seepage velocity, since macroscopic flow equations are formulated with respect to the seepage velocity.

Since $\boldsymbol{u}$ is spatially periodic and $\boldsymbol{u}$ is related to ∇p by (3.2), ∇p must be spatially periodic as well. The velocity is driven by a macroscopic homogeneous pressure gradient (average pressure gradient) $\overline{\boldsymbol{G}}$, and the pressure is given by

$$p(\boldsymbol{R}) = p_0 + \check{p}(\boldsymbol{R}) + \overline{\boldsymbol{G}} \cdot \boldsymbol{R}, \tag{3.8}$$

where p_0 is a reference pressure and $\check{p}(\boldsymbol{R})$ is spatially periodic.

All the pressure loss $-\overline{\boldsymbol{G}}$ or resistance is generated by local dissipation which is defined as

$$\Phi = 2\mu \boldsymbol{D} : \boldsymbol{D}, \tag{3.9}$$

where $\boldsymbol{D}$ is the rate of strain tensor, and : denotes summing over both tensor indices;

$$\boldsymbol{D} = \tfrac{1}{2}\left(\nabla \boldsymbol{u} + (\nabla \boldsymbol{u})^t\right), \tag{3.10}$$

where t denotes the transposition operator. For flow in spatially periodic porous media, there is a general relationship among the homogeneous gradient, average velocity and average viscous dissipation $\overline{\Phi}$ (Skjetne 1995)

$$\overline{\Phi} = -\overline{\boldsymbol{G}} \cdot \overline{\boldsymbol{u}}. \tag{3.11}$$

Alternatively, the pressure loss can be related to the forces (Skjetne 1995)

$$-\overline{\boldsymbol{G}} = -\frac{\mu}{\phi}\overline{\nabla^2 \boldsymbol{u}} + \frac{1}{\tau_f}\int_{\partial\tau_{fs}} \check{p}\mathrm{d}\boldsymbol{s} = -\frac{\mu}{\tau_f}\int_{\partial\tau_{fs}} \mathrm{d}\boldsymbol{s} \cdot \nabla \boldsymbol{u} + \frac{1}{\tau_f}\int_{\partial\tau_{fs}} \check{p}\mathrm{d}\boldsymbol{s}, \tag{3.12}$$

where $\boldsymbol{s}$ is the area directed out of the fluid.

4. Macroscopic flow equations

Flow in a porous medium is usually described by relations between the average pressure gradient and the average velocity. In our case, the average velocity in the y-direction vanishes, so one-dimensional macroscopic flow equations are sufficient. For vanishing inertia, $Re \to 0$, the flow is described by Darcy's law, which is a solution

of the Navier–Stokes equations with the inertial term set equal to zero, i.e. a solution of the Stokes equation

$$-\overline{G} = \frac{\mu}{K}\overline{u}. \tag{4.1}$$

For weak inertia, it may be shown theoretically by using a homogenization technique (perturbation theory) that for isotropic homogeneous porous media the correction to Darcy's law is a third-order term in velocity (Mei & Auriault 1991; Wodie & Levy 1991):

$$-\overline{G} = \frac{\mu}{K}\overline{u} + b\overline{u}^3, \tag{4.2}$$

where b is a parameter for the nonlinear term. Wodie & Levy (1991) explicitly stated that

$$b = \frac{c\rho^2}{K^4\mu}, \tag{4.3}$$

where c is only dependent on the geometry of the porous medium. Since K is also only dependent on the geometry of the porous medium, it seems natural to combine these parameters into one dimensionless parameter, $\gamma = c/K^4$. With this notation, the weak inertia equation can be written

$$-\overline{G} = \frac{\mu}{K}\overline{u} + \frac{\gamma\rho^2}{\mu}\overline{u}^3. \tag{4.4}$$

Although self-affine surfaces have no characteristic length scales, except their lower and upper cutoffs, one should not doubt results from perturbation theory where two characteristic length scales are used. The vertical spacing L_p introduces a microscopic scale and a macroscopic pressure loss scale is ensured by using a periodic medium.

Strong inertia is usually described by the empirical Forchheimer equation

$$-\overline{G} = \frac{\mu}{K_{fh}}\overline{u} + \beta\rho|\overline{u}|\overline{u}, \tag{4.5}$$

where β is the so-called inertial resistance (or inertial coefficient) and K_{fh} is a Forchheimer permeability. Traditionally, it is assumed that K_{fh} is equal to K. Since the shape of the flow field may change very much from vanishing to strong inertia, we do not, at this stage, see any particular reason why K_{fh} should be equal to K. Accordingly, we assume that in general $K_{fh} \neq K$. However, we will later argue that they are quite similar. Since the weak and strong inertia regimes are described by different flow equations it is reasonable to assume that there is a crossover regime between them where neither of the two flow equations is strictly valid.

In fluid mechanics it is common practice to analyse inertial flow in terms of an average Reynolds number $\overline{Re}$ instead of the average velocity $\overline{u}$

$$\overline{Re} = \frac{\rho L_p|\overline{u}|}{\mu}. \tag{4.6}$$

Note that the fluid-averaged (interstitial) Reynolds number

$$Re^* = \overline{Re}/\phi \tag{4.7}$$

is larger and closer to the local Re than $\overline{Re}$. Working with $\overline{Re}$ as flow variable instead of $\overline{u}$, we obtain the following for the Darcy, the weak inertia and the Forchheimer

equations:

$$-\overline{G} = \frac{\mu^2}{K\rho L_p}\overline{Re}, \tag{4.8}$$

$$-\overline{G} = \frac{\mu^2}{K\rho L_p}\overline{Re} + \frac{\gamma\mu^2}{\rho L_p^3}\overline{Re}^3, \tag{4.9}$$

and

$$-\overline{G} = \frac{\mu^2}{K_{fh}\rho L_p}\overline{Re} + \frac{\beta\mu^2}{\rho L_p^2}\overline{Re}^2. \tag{4.10}$$

Using u^* or Re^* as flow variable results in the following parameters:

$$K^* = \phi^{-1}K, \quad \gamma^* = \phi^3\gamma, \quad \beta^* = \phi^2\beta. \tag{4.11}$$

To better visualize the increased resistance due to inertia, we express the pressure loss in terms of an effective permeability $K_e(\overline{Re})$ defined by

$$K_e(\overline{Re}) = \frac{\mu\overline{u}}{-\overline{G}}. \tag{4.12}$$

For Darcy's law K_e is independent of $\overline{Re}$:

$$K_e = K. \tag{4.13}$$

For the weak inertia K_e is dependent on $\overline{Re}$:

$$K_e = \frac{K}{1 + (\gamma K/L_p^2)\overline{Re}^2}. \tag{4.14}$$

By rearranging this equation into (Barrère 1990)

$$\left(\frac{1}{K_e} - \frac{1}{K}\right)\frac{1}{\overline{Re}} = \frac{\gamma}{L_p^2}\overline{Re}, \tag{4.15}$$

and then plotting the left-hand side of this equation *vs.* $\overline{Re}$, the data described by the weak inertia equation follow a straight line with zero intercept.

For strong inertia, the permeability is given by

$$K_e(\overline{Re} = 0) = K_{fh}, \tag{4.16}$$

so that

$$K_e = \frac{K_{fh}}{1 + (\beta K_{fh}/L_p)\overline{Re}} \tag{4.17}$$

or for the effective resistance

$$\frac{1}{K_e} = \frac{1}{K_{fh}} + \frac{\beta}{L_p}\overline{Re}. \tag{4.18}$$

If the data follow the Forchheimer equation for strong inertia, a plot of $1/K_e$ versus $\overline{Re}$ for strong inertia (large $\overline{Re}$) should result in a straight line with intercept at $1/K_{fh}$. To visualize the crossover from weak to strong inertia, it is useful to rearrange the Forchheimer equation in the same way as the left-hand side of (4.15):

$$\left(\frac{1}{K_e} - \frac{1}{K}\right)\frac{1}{\overline{Re}} = \frac{\beta}{L_p} + \frac{K - K_{fh}}{KK_{fh}\overline{Re}}. \tag{4.19}$$

In the limit $\overline{Re} \to \infty$, the right-hand side of (4.19) becomes β/L_p.

5. Numerics

A point-iterative, finite-difference, artificial compressibility method on a staggered grid was used to solve the Navier–Stokes equations (Peyret & Taylor 1983). An important feature of this method is that the constraint (3.1) is not fulfilled during a transitional stage. The lack of mass balance is used to correct the pressure field by the following expression:

$$\frac{\partial p}{\partial t} + C^2 \nabla \cdot \boldsymbol{u} = 0, \tag{5.1}$$

where C is a positive parameter. When (5.1) converges, the velocity field is divergence free. For the momentum balance, the time-dependent Navier–Stokes equations are discretized and solved:

$$\rho \frac{\partial \boldsymbol{u}}{\partial t} = -\rho \nabla \cdot (\boldsymbol{u}\boldsymbol{u}) - \nabla p + \mu \nabla^2 \boldsymbol{u}. \tag{5.2}$$

Details on the discretization method, boundary conditions, stability criteria, the code together with testing results are given in Skjetne (1995). A simulation starts by applying a pressure gradient $\overline{G}$ to a zero velocity field. The average velocity is computed by simply summing all the cell velocities for each component, and the average pressure gradient is the one that is applied to the system.

The permeability is obtained by solving the Stokes equations. For weak inertia, we use central differences for the nonlinear term in conservative form in the Navier–Stokes equations $\nabla \cdot \boldsymbol{u}\boldsymbol{u}$, and for strong inertia we discretized the nonlinear term in non-conservative form (convective form) $\boldsymbol{u} \cdot \nabla \boldsymbol{u}$ and use second-order upwind differentiation for the derivative part and linear interpolation for the first $\boldsymbol{u}$. All fluid/solid configurations are treated separately to obtain higher-order discretization near the fracture walls. To analyse the small increase in effective flow resistance, we let the effective permeability converge with the convergence threshold (Skjetne 1995) set to 10^{-10}. For convenience we have used

$$\mu = \rho = \Delta x = 1. \tag{5.3}$$

6. Microscopic description

We have done more than 100 simulations of velocity and pressure fields in the fracture. The average Reynolds number ranges from 0 to 52. For average Reynolds numbers less than unity, we have chosen to use the central difference for the convective terms, and for larger average Reynolds numbers we have used upwind discretization for the convective terms. The central difference scheme has also been tested for larger Reynolds numbers, but tends to be less stable and gives in general a higher pressure loss for the same rate than the upwind code. The difference in pressure gradient in the two schemes is about 20% for $\overline{Re} = 33$, but decreases for smaller average Reynolds numbers. In total, 27 simulations with the central difference scheme, and 33 simulations with the upwind scheme are presented. In this section, however, we will concentrate on the flow behaviour for a few average Reynolds numbers.

In this section, velocity and pressure fields are described on a microscopic scale in different ways. This is done to better our understanding of flow and pressure loss mechanisms which contribute to the relationships between average velocity and average pressure gradient. A macroscopic analysis of these relationships is done in the next section.

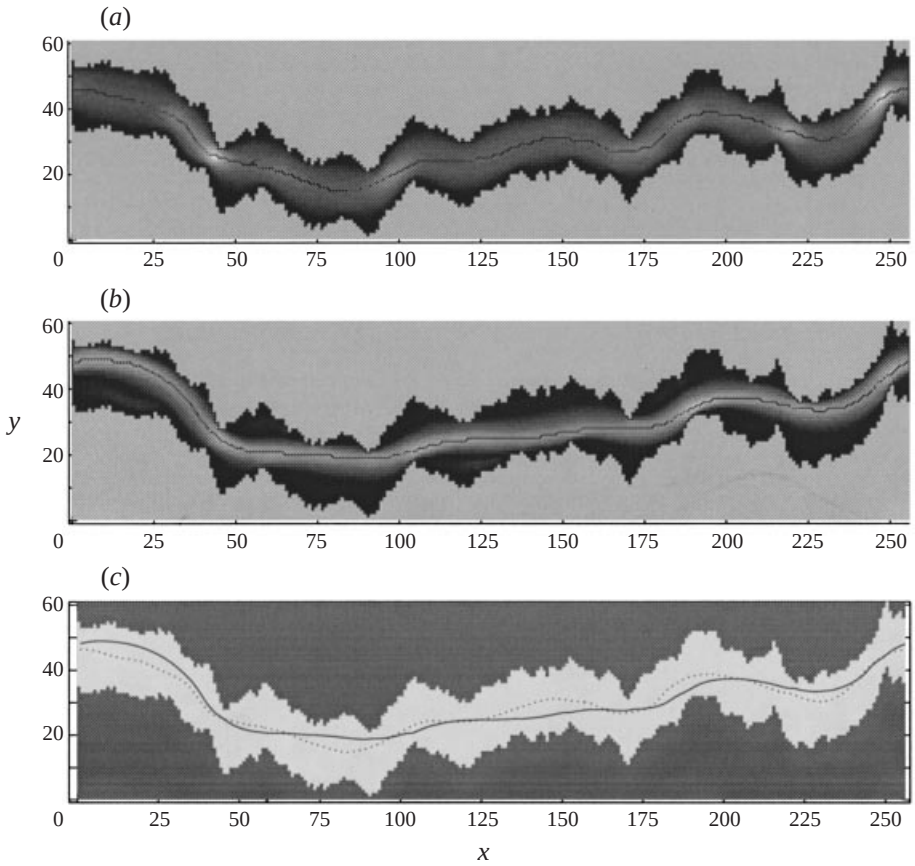

FIGURE 2. Absolute value of the velocity fields for (*a*) $\overline{Re} = 0$ and (*b*) $\overline{Re} = 52$. (*c*) Trajectories of the maximum velocity for $\overline{Re} = 0$ (dotted line) and $\overline{Re} = 52$ (solid line).

6.1. *Absolute velocity field*

We have constructed a plot which displays the shape of the main stream of the flow field. In this plot the absolute value of the velocity vector field $|\boldsymbol{u}|$ is plotted with a grey-scale (white corresponds to highest absolute value). To enhance the visualization of the main stream, a black line connects grid cells with maximum absolute velocity in neighbouring vertical columns. The black line approximately follows the main stream through the fracture. We present in figure 2(*a*) the Stokes solution (vanishing inertia or $\overline{Re} = 0$) and in figure 2(*b*) the Navier–Stokes solution with the highest Reynolds number, $\overline{Re} = 52$. A smoother maximum velocity trajectory for $\overline{Re} = 0$ and $\overline{Re} = 52$ is plotted in figure 2(*c*). For each column, the vertical position of the second-order interpolated maximum velocity (using the cell of maximum velocity and its two nearest neighbours in each column) is plotted. The absolute velocity of the not interpolated trajectory is plotted versus x in figure 3. To better visualize the overall topology of the velocity field we have constructed histograms showing absolute velocity distribution functions (figures 4 and 5).

For vanishing inertia, figure 2(*a*), the main stream is smooth and fills the central parts of the fracture. The main stream resembles a balloon that is compressed between the fracture opening. The fracture is effectively narrowest (smallest effective width) where there are large diagonally opposite peaks acting like short sloped channels

(figure 1*b*), such as for the following indices along the x-direction: 40, 95, 220 and 250. At these x positions, the absolute velocity is maximal. This is certainly due to mass balance.

The troughs play a very different role than the peaks, as they are not constricting the main stream. Instead they are located peripherally to the central parts of the fracture. They are sheltered by the peaks and form backwaters not filled by the main stream. At some places, the distance between the fracture walls normal to the main stream flow direction is larger than the effective fracture width defined in figure 1(*b*), since the absolute value of the slope of the main stream is smaller than the average slope of the fracture walls. At $x = 50\,\Delta x$ the distance between fracture walls normal to the main stream flow direction is even larger than the profile spacing ($20\,\Delta x$) and approaches the longest diagonal defined by (2.9), since the sign of the slope of the main stream flow is opposite to that of the average slope of the fracture wall around that position.

It is seen in figure 2(*b*) that the shape of the high-velocity part of the field resembles a narrow tube with essentially constant thickness which is close to the thickness of the narrowest openings normal to the flow tube. The flow tube takes short cuts and follows only partly the local shape of the fracture. At obstructions, such as for $x = 190\,\Delta x$, the flow tube has a tendency to impinge on the fracture wall and change direction. Between the flow-tube/fracture-wall contact points, the flow tube follows straight sections. The almost constant thickness of the flow tube results from convective transport of momentum which dominates over diffusional transport of momentum perpendicular to the flow tube. Also, strong inertia leads to the flow tube impinging on the fracture wall.

6.1.1. *Maximum absolute velocity trajectory*

The trajectories of the maximum velocity are plotted in figure 2(*c*) for $\overline{Re} = 0$ (dotted line) and $\overline{Re} = 52$ (solid line). It is seen that the low-velocity trajectory follows the central parts of the fracture. By comparison, the high-velocity trajectory is closer to the fracture wall, especially at positions where the flow tube tends to impinge on the fracture wall. In some regions, the high-velocity flow trajectory is longer than the low-velocity flow trajectory, such as for $0 \leqslant x \leqslant 40\,\Delta x$, where the high-velocity flow tube seems to be squeezed against the outer fracture wall in the curve. At positions where there is no apparent downstream constriction for the flow tube, the high-velocity flow trajectory is straighter (shorter) than the low-velocity flow trajectory. In the narrowest constrictions the positions of the trajectories for low and high velocities coincide.

An estimate for the tortuosity is made by calculating the length of the maximum absolute velocity trajectory, L_e. This length is calculated for different Reynolds numbers and is compared to other lengths in the system in table 1. In the table 'Profile, absolute' stands for the absolute length ('taxi cab' norm) of the roughness profile and 'Profile midpoints' stands for the sum of distances between the midpoints (Euclidean norm). In the calculation of these norms, the periodicity at the unit cell boundaries is taken into account. It is interesting to note that $L_e(\overline{Re} = 52) < L_e(\overline{Re} = 0)$. This does not support a hypothesis that an increase in flow tortuosity with Reynolds number is responsible for extra resistance (Firoozabadi & Katz 1979). Our observation is not in conflict with the common belief that high-velocity resistance is highly dependent on the tortuosity of the pore geometry.

The reduction in L_e in the interval from $\overline{Re} = 4$ to $\overline{Re} = 15$ is $3.1\,\Delta x$ while from $\overline{Re} = 15$ to $\overline{Re} = 52$ the reduction is only $1.4\,\Delta x$. Even though the latter interval of

$\overline{Re}$	L_e [Δx]	L_e/nx	$L_e - nx$ [Δx]
0	278.35	1.087	22.35
4	278.51	1.088	22.51
15	275.45	1.076	19.45
52	274.04	1.070	18.04
Profile, absolute	526	2.055	270
Profile, midpoints	404	1.578	148
Unit cell, nx	256	1	0

TABLE 1. Length of maximum velocity trajectory, L_e, and roughness profile.

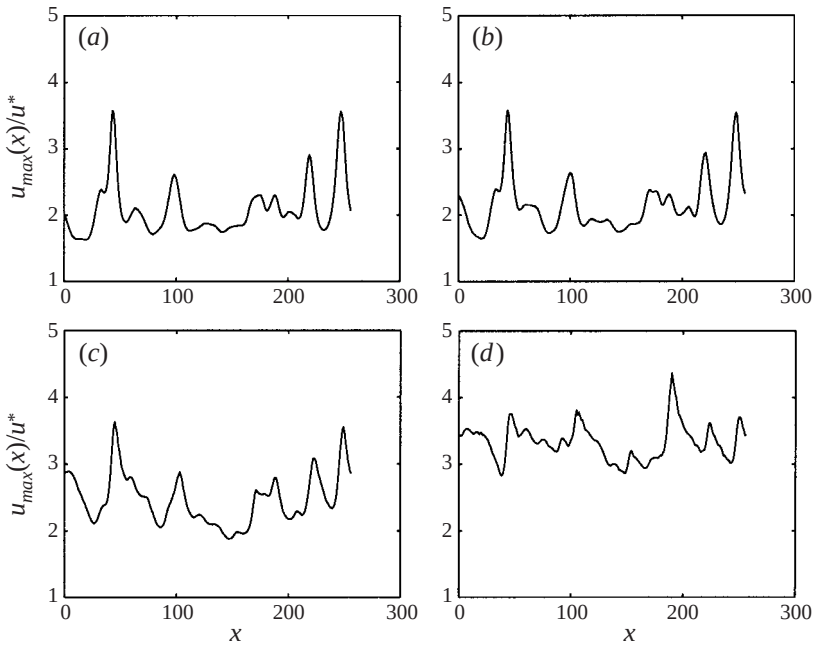

FIGURE 3. The velocity on the maximum absolute velocity trajectory in units of the interstitial velocity versus x for (*a*) $\overline{Re} = 0$, (*b*) $\overline{Re} = 4$, (*c*) $\overline{Re} = 15$, and (*d*) $\overline{Re} = 52$. The actual trajectories for $\overline{Re} = 0$ and $\overline{Re} = 52$ are displayed in figure 2.

Reynolds numbers is more than 3 times larger than the former, the reduction of L_e for the former is about twice of the reduction for the latter. From $\overline{Re} = 0$ to $\overline{Re} = 4$ there is virtually no change in L_e. Based on this, it seems that the largest changes in the velocity field are from $\overline{Re} = 4$ to $\overline{Re} = 15$.

The absolute velocity at the maximum absolute velocity trajectory is shown for (*a*) $Re = 0$, (*b*) $Re = 4$, (*c*) $Re = 15$ and (*d*) $Re = 52$ in figure 3. The velocity is in units of the interstitial velocity u^*:

$$u^* = \overline{u}/\phi. \tag{6.1}$$

These plots give some interesting information about the velocity fluctuations along the flow tube. For $\overline{Re} = 0$ and $\overline{Re} = 4$ the plots are very similar. High-velocity peaks are located at the narrowest constrictions. The peaks are rather symmetric in shape and the highest is at about $3.8\,u^*$. The peaks extend up from a velocity base level

of about $1.8\,u^*$, so that the relative height of the highest peaks is about $1.8\,u^*$. In other words, there is an intense and localized acceleration/deceleration (in space) of the main stream near the narrowest constrictions. In comparison, a straight channel would have a constant maximal velocity equal to $1.5\,u^*$. The shape of the curve for $\overline{Re} = 15$ is somewhat in between the shape of the curves for $\overline{Re} = 0$ and $\overline{Re} = 52$, so we describe only the shape for the highest Reynolds number and compare it to the shape for the smallest Reynolds number.

There are both similarities and differences between the velocity curve for $\overline{Re} = 0$ and $\overline{Re} = 52$. For $\overline{Re} = 52$, the base level of the velocity is about $3.0\,u^*$, which is more than one unit more than for $\overline{Re} = 0$ and twice that of a straight channel. The position of the three highest peaks for $\overline{Re} = 0$ is almost the same as for $\overline{Re} = 52$, but the height relative to the base level is reduced. For $\overline{Re} = 52$, the absolute height of the highest peaks, e.g. the one at $x = 250\,\Delta x$, is only about $0.1\,u^*$ higher than for vanishing inertia. As a consequence, the reduction in the height of the peaks relative to the ground level is mainly due to the increase of the base level. In brief, the mainstream acceleration/deceleration is less intense for high-velocity flow than for low-velocity flow.

Regarding the height and position of peaks, the highest peak for $\overline{Re} = 52$ at $x = 190\,\Delta x$ is virtually absent for $\overline{Re} = 0$. This can be qualitatively explained as follows: because of the inertia, the flow tube is pressed against the obstruction, the flow tube is compressed and as a result of the required mass balance, the flow tube accelerates. The same type of phenomenon can be seen in the peak at $x = 100\,\Delta x$ for $\overline{Re} = 0$, which for $\overline{Re} = 52$ has moved to a position somewhat further downstream. This can be understood by comparing figures 2(*a*) and 2(*b*), where it is seen that for $\overline{Re} = 0$ the peaks around the position $x = 100\,\Delta x$ form the narrow constriction which leads to acceleration/deceleration by mass balance, while for $\overline{Re} = 52$ the right-most peak forms an obstruction which the flow tube is pressed against.

With respect to peak shape, it is also seen in general that the peaks for $\overline{Re} = 52$ have no upstream–downstream symmetry. All the peaks are skewed, with a steep acceleration on the upstream side and with a smeared out tail on the downstream side. Physically, this asymmetry may be explained by the high-velocity spots being swept downstream by convection. Mathematically, the Navier–Stokes equations are convection/diffusion equations (with a source) for the transport of momentum and it is the dominance of convection over diffusion that results in the high-velocity tail.

In brief, the most striking aspects of high-velocity as compared to low-velocity trajectories are: (i) the high-velocity trajectory is shorter than the low velocity-trajectory, (ii) near obstructions the high-velocity trajectory is closer to the fracture wall than the low-velocity trajectory and for high-velocity the velocity is peaked, (iii) in the narrowest constrictions both the scaled maximum absolute velocity and the position of the velocity trajectory are almost the same for low-velocity and high-velocity flow.

6.1.2. *Absolute velocity distribution*

The previous discussion demonstrated that the base level of the maximum absolute velocity is not proportional to the interstitial velocity. To check if this is part of a general trend, we now study the distribution (histogram) of absolute velocity. To provide a reference, we first study the histogram for Hele-Shaw flow, i.e. flow in a straight channel as shown in figure 4.

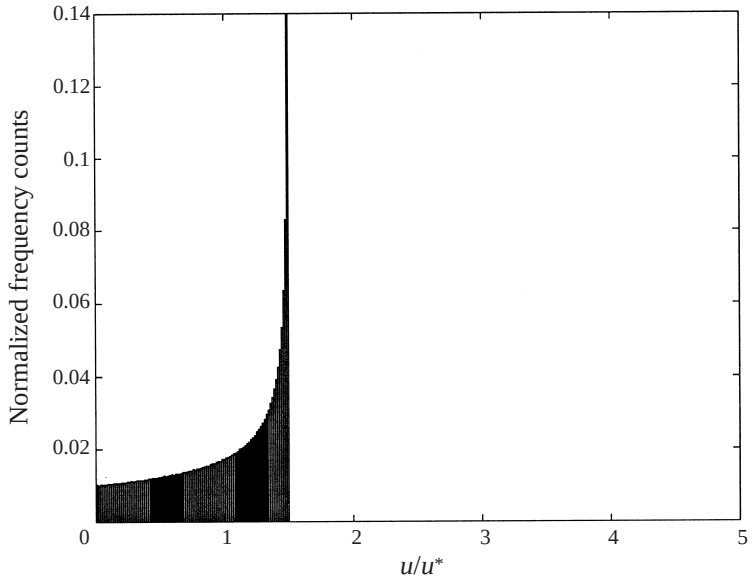

FIGURE 4. Velocity histogram for a Hele-Shaw cell. The total number of bins is 100. The sum of counts in the bins is equal to unity (normalized). The velocity axis is in units of the interstitial velocity. The counts in the the last bin is 0.2.

The histogram is constructed from the velocity profile

$$u_d = \tfrac{3}{2}(1 - y_d^2), \quad \forall\ y_d \in (-1, 1), \tag{6.2}$$

where $u_d = u/u^*$ and $y_d = 2y/L_p$; $u^*(= \frac{2}{3}u(0) = \frac{2}{3}u_{max})$ is the interstitial velocity, L_p is the channel width, and y is the height relative to the centre of the channel. Each bin in a histogram is an interval in u_d. The size of the intervals is constant. The shape in figure 4 is given by the resulting increments in y_d, which scales as the absolute value of the derivative of y_d with respect to u_d:

$$\left|\frac{\partial y_d}{\partial u_d}\right| \sim (1 - \tfrac{2}{3}u_d)^{-1/2} = \begin{cases} 1 + \frac{1}{3}u_d & \text{for } u_d \ll \frac{3}{2} \\ \to \infty & \text{for } u_d \to \frac{3}{2}. \end{cases} \tag{6.3}$$

Histograms for the rough fracture are shown in figure 5, for (*a*) $\overline{Re} = 0$, (*b*) $\overline{Re} = 4$, (*c*) $\overline{Re} = 15$ and (*d*) $\overline{Re} = 52$. The histogram for $\overline{Re} = 0$ (figure 5*a*) has two peaks: one for zero velocity and one for about $1.8\,u^*$. The position of the last peak is similar to the base level in figure 3(*a*). The first peak is sharper and higher than the second peak. For high velocities, the distribution function falls off with a maximum for about $3.7\,u^*$, which is the same as the velocity of the highest peaks in figure 3(*a*).

In comparison, the first peak is not seen for the Hele-Shaw cell. It is a result of low-velocity flow in peripheral troughs. The second peak resembles the peak for the Hele-Shaw cell, but is shifted towards a higher velocity and is smeared out. The shift is due to two effects. First, low velocity in peripheral troughs results in a low interstitial velocity in the normalization, and second a local velocity in the y-direction contributes to the absolute velocity field, but not to the interstitial velocity. Smearing of the second peak is due the variation of effective width L_w in the fracture.

The histogram for $\overline{Re} = 4$ is similar to that of $\overline{Re} = 0$, except for the first peak for zero velocity which has increased. From $\overline{Re} = 4$ to $\overline{Re} = 15$ the low-velocity peak has

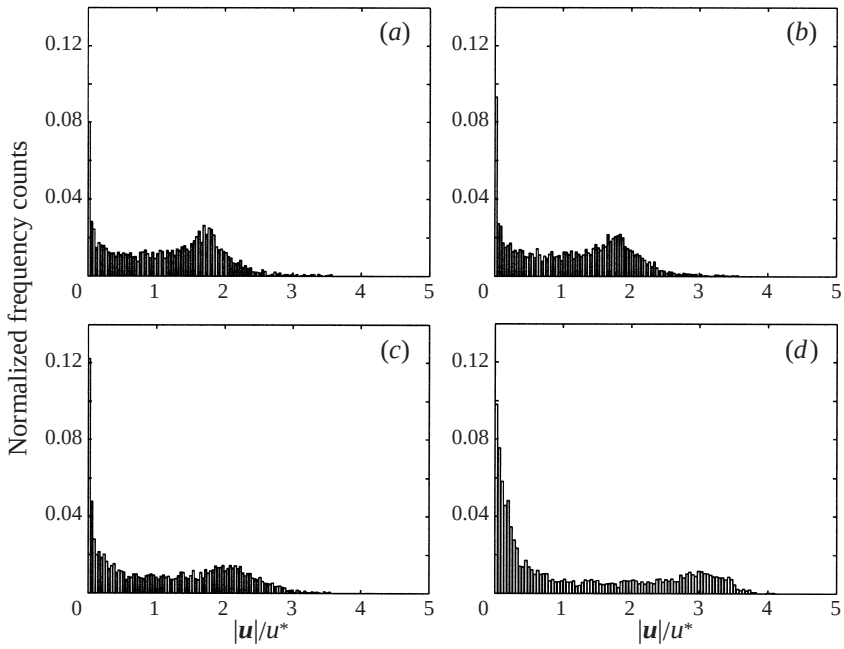

FIGURE 5. Velocity histogram for the self-affine fracture for (*a*) $\overline{Re} = 0$, (*b*) $\overline{Re} = 4$, (*c*) $\overline{Re} = 15$ and (*d*) $\overline{Re} = 52$. The total number of bins is 100. The sum of counts in the bins is equal to unity (normalized). The velocity axis is in units of the interstitial velocity.

become higher and broader. The high-velocity peak is lower and shifted to higher velocities. For $\overline{Re} = 52$ the area of the first peak has increased, and the second peak is further shifted to a velocity of about $3.0\,u^*$, which corresponds to the base level in figure 3(*d*). The density of intermediate velocities is reduced. To sum up, there is a strong segregation of velocities with increasing Reynolds number, and the velocity in the flow tube increases much faster than the interstitial velocity. This is a general effect which may explain some of the increased pressure loss for high-velocity flow in porous media.

6.1.3. *Velocity vector fields*

To better visualize details of low- and high-velocity fields, velocity vector fields are presented for $\overline{Re} = 0$ and $\overline{Re} = 52$ in figure 6 and figure 7, respectively. The figures cover the fracture from left to right. The two velocity fields are very different. For $\overline{Re} = 0$, it is seen that the velocity field does not fill the deepest troughs, but fills other parts quite well. For $\overline{Re} = 52$, the backwater regions are much larger than for low velocity, and the high-velocity flow tube is clearly seen. The high-velocity tube drives low-velocity vortices in backwaters, such as the large recirculation zone below the flow tube for $0 < x < 30\,\Delta x$.

Transversal narrowing of the flow tube is observed at some peaks, e.g. for the peaks at $x = 153\,\Delta x$ and $x = 170\ \Delta x$. The peaks peel off the outer layer of the flow tube, and help keep an almost constant thickness of the flow tube. Between such peaks, in open space, the flow tube broadens slightly. This broadening effect may be viewed as a transversal diffusion effect of the viscous term in the Navier–Stokes equation. A flow tube impinging on the fracture wall is seen for about $x = 185\,\Delta x$. At this

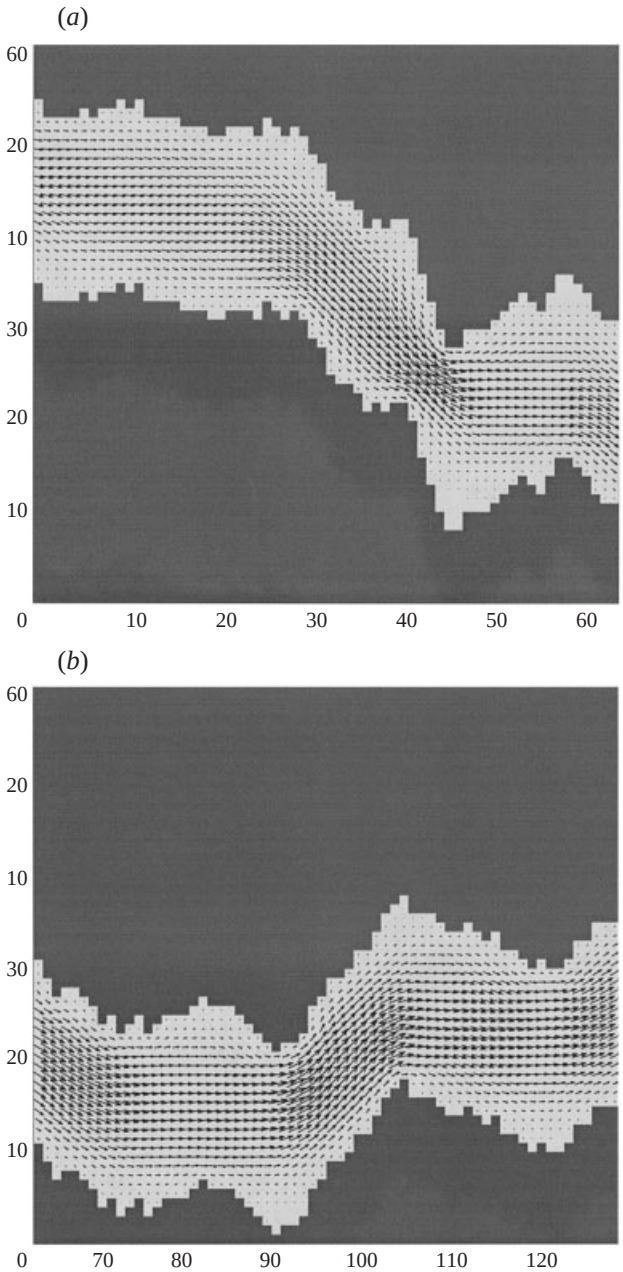

FIGURE 6(*a*, *b*). For caption see facing page.

position the flow tube comes very close to the fracture wall. It will be seen in the next subsection that this impinging leads to a large pressure loss.

6.2. *Pressure field*

Pressure fields for $\overline{Re} = 0$ and $\overline{Re} = 52$ are plotted as three-dimensional surfaces with lighting in figures 8(*a*) and 8(*b*). The pressure field for $\overline{Re} = 0$ falls off smoothly in the x-direction, and with the largest pressure losses where the effective width is smallest.

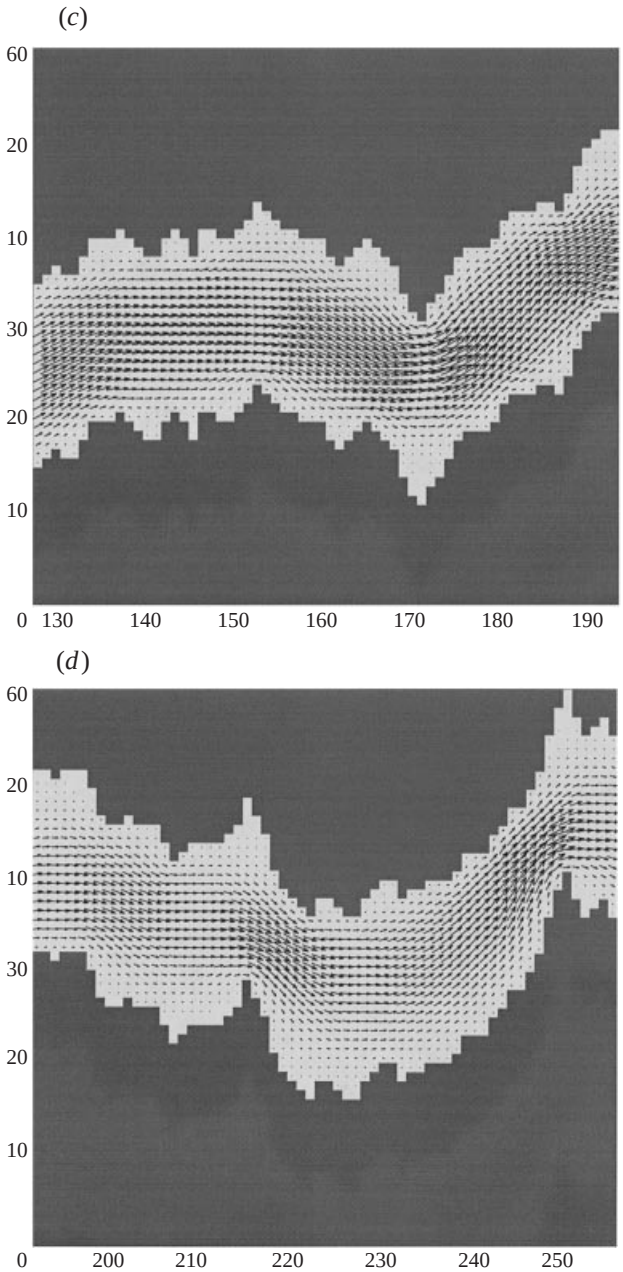

FIGURE 6. Velocity vector fields for $\overline{Re} = 0$ for (*a*) $0 \leqslant x \leqslant 64\,\Delta x$, (*b*) $64\Delta x \leqslant x \leqslant 128\Delta x$, (*c*) $128\Delta x \leqslant x \leqslant 192\Delta x$, (*d*) $192\Delta x \leqslant x \leqslant 256\Delta x$. The maximum size of the vectors in each plot is equal to the size of three grid cells.

The narrowest constrictions do not, however, dominate the pressure loss completely. Note that for vanishing inertia all the pressure loss is dissipative.

For $\overline{Re} = 52$ the pressure field is much more varied, and not all the local pressure loss is dissipative. In the backwaters, filled with vortices, the pressure is virtually constant, because the velocity in the recirculation region is much lower than in

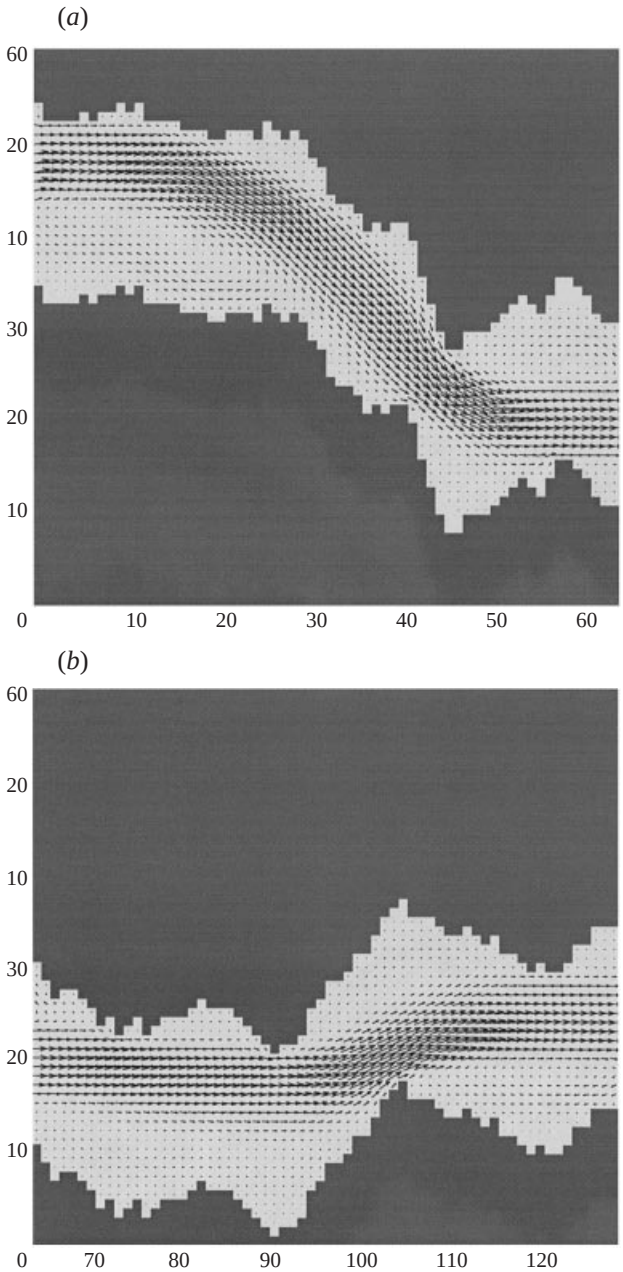

FIGURE 7(*a*, *b*). For caption see facing page.

the flow tube. Even though the vortices are eye-catching on a velocity vector plot, they do not contribute to the pressure loss. There are regions with pressure loss perpendicular to the flow tube, such as for $x < 30\,\Delta x$. In these regions part of the pressure gradient almost certainly provides the centripetal force needed to bend the flow tube. This effect is essentially non-dissipative since the flow resembles solid-body rotation for which there is no dissipation. In the narrowest constrictions the largest pressure losses are found. These losses are partly non-dissipative and partly

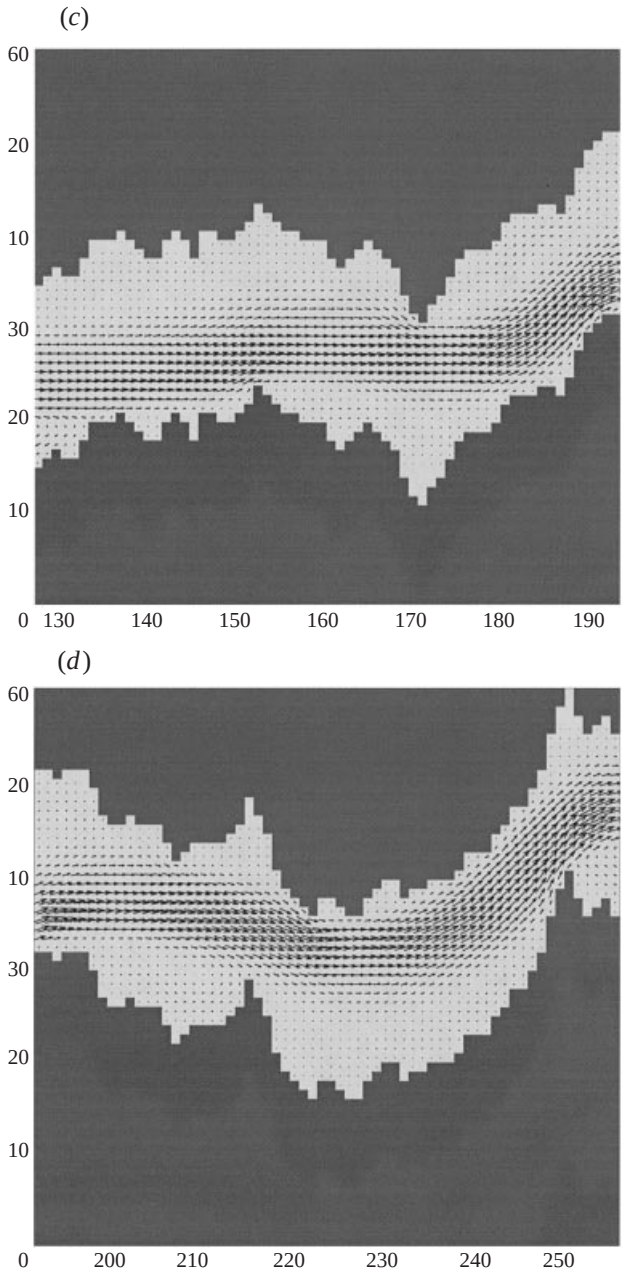

FIGURE 7. Velocity vector fields for $\overline{Re} = 0$ for (*a*) $0 \leqslant x \leqslant 64\Delta x$, (*b*) $64\Delta x \leqslant x \leqslant 128\Delta x$, (*c*) $128\Delta x \leqslant x \leqslant 192\Delta x$, (*d*) $192\Delta x \leqslant x \leqslant 256\Delta x$. The maximum size of the vectors in each plot is equal to the size of three grid cells.

dissipative. The non-dissipative loss is due to acceleration of the flow tube (figure 3), because of the possible non-dissipative exchange between kinetic energy and pressure, i.e. the Bernoulli effect. The Bernoulli effect can be seen mathematically by writing the Navier–Stokes equation on the alternative form

$$\nabla(p + \rho\tfrac{1}{2}|\boldsymbol{u}|^2) = \rho\boldsymbol{u} \times \boldsymbol{\omega} - \mu\nabla \times \boldsymbol{\omega}, \tag{6.4}$$

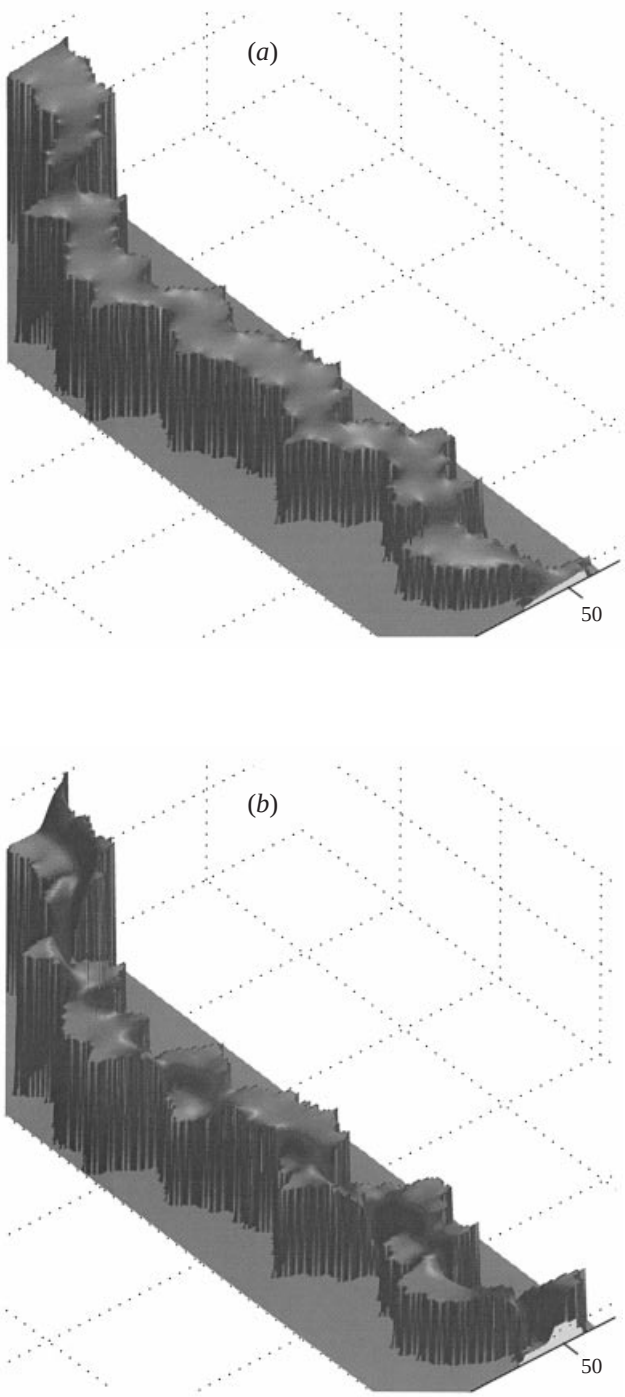

FIGURE 8. Normalized pressure field for (*a*) $\overline{Re} = 0$, (*b*) $\overline{Re} = 52$.

where $\boldsymbol{\omega} = \nabla \times \mathbf{u}$ is the vorticity. For irrotational flow, $\boldsymbol{\omega} = \mathbf{0}$, there may be a non-dissipative exchange between pressure and kinetic energy in the flow direction. Dissipative pressure loss mechanisms are discussed in § 8.

In figure 9 normalized pressure profiles (average pressure in each vertical column)

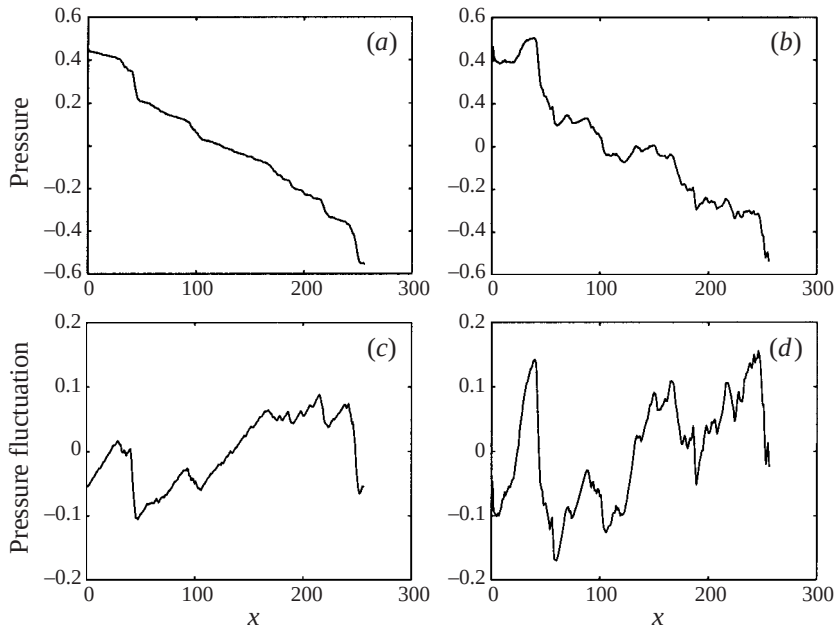

FIGURE 9. Normalized pressure profiles (average pressure in each vertical column) for (*a*) $\overline{Re} = 0$, (*b*) $\overline{Re} = 52$, and the pressure fluctuation $\breve{p}$ in units of the total pressure loss for (*c*) $\overline{Re} = 0$ and (*d*) $\overline{Re} = 52$.

K [Δx^2]	K_{fh} [Δx^2]	γ[1]	β [1/Δx]
2.82	2.964	1.042	0.2387

TABLE 2. Parameters obtained from least squares fits

for (*a*) $\overline{Re} = 0$, (*b*) $\overline{Re} = 52$, and the pressure fluctuation $\breve{p}$ in units of the total pressure loss for (*c*) $\overline{Re} = 0$ and (*d*) $\overline{Re} = 52$, are presented to better visualize the pressure change along the fracture. Note that for the pressure fluctuations (figure 9*c* and 9*d*), a positive slope means less pressure loss than on average and a negative slope more pressure loss than on average. For $\overline{Re} = 0$ it is seen that the derivative of the pressure in the x-direction is always negative, and it is most negative at the narrowest constrictions. For $\overline{Re} = 52$, the derivative of the pressure in the x-direction is somewhere positive. The reason for this pressure increase may partly be that it balances the centripetal acceleration, but it is more likely that the pressure increases because the flow tube decelerates due to the Bernoulli effect. By comparing figure 9(*b*) and 9(*d*) with figure 3(*d*) it is seen that the largest pressure increase is correlated with the largest deceleration of maximum absolute velocity trajectory.

7. Macroscopic analysis

The results of the fits are summarized in table 2. The parameters based on interstitial velocity or Reynolds number, (4.11) with $\phi = 0.328$, are given in table 3. In brief, we have found that the data are well described by Darcy's law, the weak inertia equation

K^* [Δx^2]	K^*_{fh} [Δx^2]	γ^*[1]	β^* [$1/\Delta x$]
8.60	9.037	3.677×10^{-2}	2.568×10^{-2}

TABLE 3. Parameters based on interstitial velocity obtained from least squares fits

and the Forchheimer equation for no inertia, weak inertia and strong inertia, respectively, and that there is a crossover between the weak and strong inertial flow regimes.

7.1. *Permeability*

It is interesting to compare the simulated K, with a K estimated from the geometry of the fracture. The permeability was calculated to be $K = 2.82$. The smallest effective width is found at about $x = 45\,\Delta x$, where the effective width is about $7\,\Delta x$, and the largest pressure loss is found there.

The fracture can be viewed as a serial coupling of N fractures with effective widths $L_{w,i}$ and length along the flow path Δx_i. For simplicity we can assume that each section has a permeability given by the permeability of a straight fracture with width equal to $L_{w,i}$, so that Darcy's law for section i can be written

$$-\left(\frac{\mathrm{d}p}{\mathrm{d}x}\right)_i = \frac{12\mu}{L^2_{w,i}}\overline{u}_{p,i} = \frac{12\mu}{L^3_{w,i}} w_{tot}\overline{u}, \tag{7.1}$$

where $\overline{u}_{p,i}$ is the average velocity in fracture number i, and the total height of the model w_{tot} is $61\,\Delta x$. The total pressure loss over the length of the model L_u is then

$$-\frac{\Delta p}{L_u} = \sum_i \frac{12\mu w_{tot}}{L^3_{w,i}} \frac{\Delta x_i}{L_u}\overline{u}, \tag{7.2}$$

so that the permeability of the medium becomes

$$K = \left(\frac{L_u}{12 w_{tot}} \sum_i \frac{\Delta x_i}{L^3_{w,i}}\right)^{-1}. \tag{7.3}$$

The permeability is dominated by sections with large $\Delta x_i / L^3_{w,i}$. For example, to obtain a pressure loss in the widest section $L_{w,max} = L_p = 20\,\Delta x$ equal to the narrowest $L_{w,min} = 7\,\Delta x$, the length of the widest fracture must be 23.3 ($= 20^3/7^3$) times longer than the narrowest fracture. This is in accordance with what was found in Gutfraind & Hansen (1995), Gutfraind *et al.* (1995).

With this information, an upper bound for the permeability can be estimated by using the equation for the permeability of a straight fracture of width L_p and length $nx = 256\,\Delta x$, for which

$$K = \tfrac{1}{12} L_p^2. \tag{7.4}$$

Taking into account the porosity, the simulated permeability is estimated as

$$K = \phi \tfrac{1}{12} L_p^2 = 10.9. \tag{7.5}$$

As expected, this permeability is higher than the simulated K.

Another way to see if the permeability is realistic is to use (7.3) and solve for a

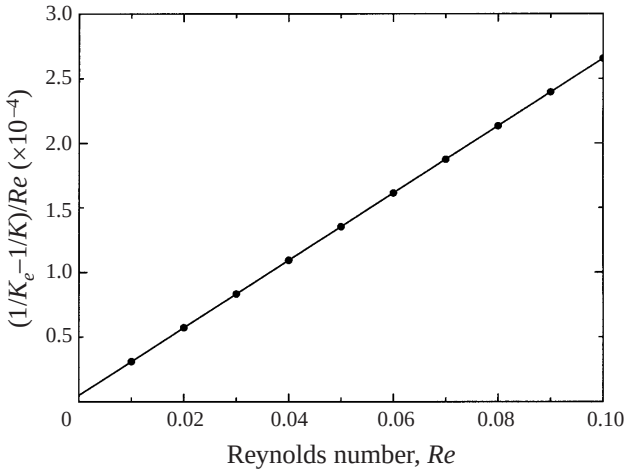

FIGURE 10. Simulation results of weak inertia. Fit of a straight line with constant a_0 and slope a_1. By using (4.15), $a_1 = \gamma/L_p^2$, it is found from the plot that $\gamma = 1.042$.

characteristic effective width $L_{w,c}$ defined by

$$\frac{1}{L_{w,c}} = \left(\frac{1}{L_e} \sum_i \frac{\Delta x_i}{L_{w,i}^3} \right)^{1/3}, \tag{7.6}$$

so that

$$L_{w,c} = \left(\frac{12 w_{tot} L_e K}{L_u} \right)^{1/3} = 13.1\,\Delta x, \tag{7.7}$$

where $L_e = 278.35\,\Delta x$ has been used. This effective width is somewhat smaller than the average of the smallest effective width $7\,\Delta x$ and L_p, $13.5\,\Delta x$.

7.2. *Weak inertia*

It is seen from the simulations that for $\overline{Re} \simeq 10^{-2}$, the relative decrease in K_e from K is only 8.76×10^{-7} and for $\overline{Re} \simeq 10^{-1}$ it is 7.48×10^{-5}. In other words, the decrease in permeability is very small. To check whether the data can be described by the weak inertia equation, we have fitted a straight line in $10^{-2} < \overline{Re} < 10^{-1}$ to the data arranged as the left-hand side of (4.15) in figure 10. It is seen that a straight line fits very well with an intercept 5.0×10^{-6} and a slope 2.6×10^{-3}. The straight line does not have zero intercept, which it should have if it followed the weak inertia equation. The constant term is, however, small, and for $\overline{Re} = 0.1$ the constant term contributes less than 2% of the total signal. For larger $\overline{Re}$ the constant is even less significant. In figure 11 the fit from figure 10 is extended up to $\overline{Re} \simeq 1.0$ and the constant term can hardly be seen at all. We therefore use the slope from the fit in figure 10, (4.15) and (2.7) to estimate the weak inertial coefficient $\gamma = 1.04$. From (4.9) and (5.3) it can be calculated that the estimated additional pressure loss due to weak inertia at $\overline{Re} = 1$ is only 0.73% of the Darcy pressure loss.

7.3. *Crossover from weak to strong inertia*

In figure 11 it is also seen that for the largest $\overline{Re}$ there is a systematic departure from the straight line. The weak inertia equation holds theoretically, at least, for $\overline{Re} \ll 1.0$. It is likely to break down for Reynolds numbers of the order of unity,

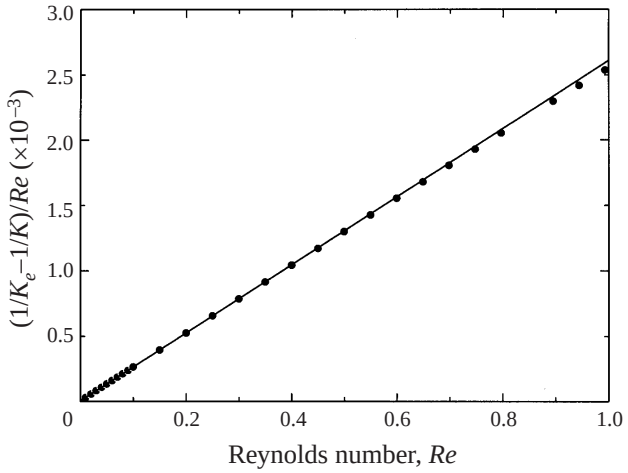

FIGURE 11. The fit from figure 10, plotted together with data for $\overline{Re} < 1.0$. Note how insignificant the constant term in the fit is on this scale.

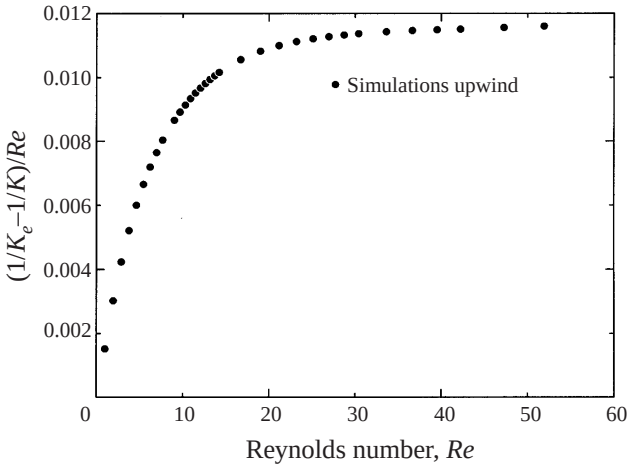

FIGURE 12. Simulation results for the crossover from weak to strong inertia.

since homogenization of the Navier–Stokes equations shows that the leading-order flow problem becomes non-linear (Sanchez-Palencia 1980; Auriault *et al.* 1990). That the trend is lower than the fit is in accordance with a crossover from the weak inertia equation to a Forchheimer equation. If the data followed a Forchheimer equation with $K_{fh} = K$, they should be constant, i.e. follow a straight line with zero slope.

To check how this crossover evolves for larger $\overline{Re}$, we plot data in the same way as in figures 10 and 11, but with $\overline{Re} > 1$, i.e. in the region where the weak inertia equation may not hold theoretically. As can be seen in figure 12 there is a crossover from a straight line with zero (not strictly) intercept to an almost constant. For high $\overline{Re}$ this result is in accordance with the Forchheimer equation formulated by (4.19). The crossover region from weak to strong inertia spans a significant interval in Reynolds number and can be approximately defined by $1 < \overline{Re} < 25$.

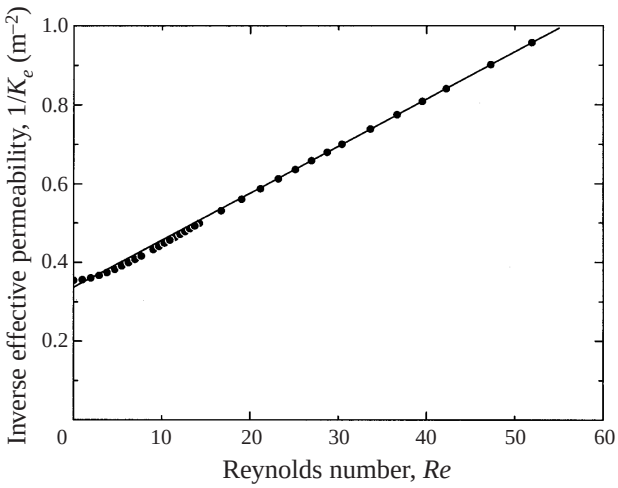

FIGURE 13. Simulation results for strong inertia. A straight line with constant a_0 and slope a_1 is fitted to the data in the range $25 \leqslant Re \leqslant 52$. From (4.10), $a_0 = 1/K_{fh}$ and $a_1 = \beta/L_p$, so that $K_{fh} = 2.964$ and $\beta = 0.2387$.

7.4. *Strong inertia*

To better check whether the strong inertia data follow Forchheimer equation, we have plotted the data according to (4.18) in figure 13, where the data for $\overline{Re} > 25$ are fitted to the Forchheimer equation. In this plot the y-axis is the effective inertial resistance $(1/K_e)$. The Forchheimer equation follows the strong inertial data well with $K_{fh} = 3.07$ and $\beta = 0.2446$. We have thus that the relative difference between K_{fh} and K is 8.8%. It is seen that $1/K_e$ is almost constant in the weak inertial regime, while $1/K_e$ is about 3 times larger than $1/K$ for the largest $\overline{Re} = 52$.

8. Discussion of pressure loss effects

To find the physical effects that contribute to the increase in the effective resistance $1/K_e$ for vanishing and strong inertia, we look at how the effective resistance may change because of the changes in the shape of the velocity field. For the Darcy flow regime, the shape of the flow field (velocity divided by e.g. the maximum velocity) is independent of $\overline{Re}$, and the resistance is independent of Reynolds number.

For inertial flow, the shape of the flow field changes with Reynolds number. The extra increase in resistance is a result of this change and in particular the changes that increase the dissipation. One such effect is the buildup of boundary layers. However, this gives a pressure loss which scales with Reynolds number as $Re^{3/2}$, and is thus not sufficient to explain the Forchheimer pressure loss. Relationships for developing flow between flat plates and in ducts have been used to model flow through consolidated and granular media (Du Plessis & Masliyah 1988, 1991), and resulted in the same power of 3/2 in the high-velocity boundary layer flow regime. We note that ideal boundary layers do not take into account any effects of flow tubes as observed in this study. Since the velocity in a flow tube increases faster than the interstitial velocity, the pressure loss for boundary layers associated with flow tube bends will be higher than for ideal boundary layers with a Reynolds number based on an average velocity. This may explain the power 2 in the Forchheimer equation. The narrowest constrictions seem to contribute most to the linear term in the Forchheimer equation

as the maximum trajectory in the flow tube does not come closer to the fracture wall with increasing Reynolds number.

9. Conclusions

Low- and high-velocity flow in a self-affine fracture with a constant perpendicular opening has been simulated by solving numerically the Navier–Stokes equations. For the Stokes solution the velocity field tends to fill the fracture. However, the most peripheral troughs of the fracture do not contribute to the transport. The diffusional character is attributed to the smoothing effect of the viscous (diffusion) term in the Stokes equations.

Strong inertia leads to three main effects: (i) the shape of the absolute velocity field resembles a narrow tube of essentially constant thickness equal to the smallest effective widths of the fracture, (ii) the flow tube has linear sections and bends where it impinges on the fracture wall, and (iii) the velocity in the flow tube increases faster than the interstitial velocity. Effect (i) results from a transversal diffusion which is weak compared to the longitudinal convection; (ii) can be explained in the same way as (i) but used for diffusion in the longitudinal direction, (iii) is a result of flow tube narrowing with increasing Reynolds number.

We argue that the Forchheimer equation can be divided in geometrically separate parts. That is, the linear contribution is dominated by the narrowest constrictions for both low- and high-velocity flow, whereas the zones where the flow tube wall impinges on the fracture wall contribute mainly to the Forchheimer term, and not particularly much to the Darcy term for low-velocity flow.

Quantitatively, vanishing, weak and strong inertial flow regimes were well described by the Darcy, weak inertia and Forchheimer flow equations, respectively. A cross-over flow regime from the weak to strong inertia is also observed.

Financial support was received from the Research Council of Norway through the non-Darcy Flow projects (426.91/063 and 111241/431) of the PROPETRO program.

REFERENCES

Abraham, F. F., Brodbeck, D., Rafey, R. A. & Rudge, W. E. 1994 Instability dynamics of fracture: A computer simulation investigation. *Phys. Rev. Lett.* **73**, 272–275.

Adler, P. M. 1992 *Porous Media*. Butterworth Heinemann.

Auriault, J.-L., Strzelecki, T., Bauer, J. & He, S. 1990 Porous deformable media saturated by a very compressible fluid: quasi-statics. *Eur. J. Mech.* A/*Solids* **9**, 373–392.

Aviles, C. A., Scholz, C. H. & Boatwright, J. 1987 Fractal analysis applied to characteristic segments of the San Andreas fault. *J. Geophys. Res.* **92**, 331.

Balberg, I. 1986 Connectivity and conductivity in 2d and 3d fracture systems. *Ann. Israel Phys. Soc.* **8**, 89.

Barabási, A. L. & Stanley, H. E. 1995 *Fractal Concepts in Surface Growth*. Cambridge University Press.

Barrère 1990 Modélisation des écoulements de Stokes et Navier-Stokes en milieu poreux. Doctoral thesis, Université de Bordeaux I.

Bouchaud, E. 1997 Scaling properties of cracks. *J. Phys. Condensed Matter* **9**, 4319.

Bouchaud, E., Lapassat, G. & Planès 1990 Fractal dimension of fractured surfaces: A universial value? *Europhys. Lett.* **13**, 73–79.

Bour, O. 1991 Analyse fractale du réseau de failles de San Andreas. Univ. Rennes 1, doctoral thesis (DEA), Université Rennes 1.

Brown, S. R. & Scholz, C. H. 1985 Broad bandwidth study of the topography of natural rock surfaces. *J. Geophys. Res.* **90**, 12575.

Chauveteau, G. 1965 Essai sur la loi de darcy et les écoulements laminaires à pertes de charge non linéaires. Docteur-Ingénieur Thesis, Faculté des Sciences de Toulouse.

Couland, O., Morel, P. & Caltagirone, J. P. 1988 Numerical modelling of nonllinear effects in laminar flow through a porous medium. *J. Fluid Mech.* **190**, 393–407.

Dauskardt, R. H., Haubensak, F. & Richtie, R. O. 1990 On the interpretation of the fractal character of fracture surfaces. *Acta Metall. Mater.* **38**, 143–159.

Davy, P. 1993 On the fault-length frequency distribution of the San Andreas fault system. *Geophys. Res.* **98**, 12414.

Davy, P., Sornette, A. & Sornette, D. 1992 Experimental discovery of scaling laws relating fractal dimensions and the length distribution exponent to fault systems. *Geophys. Res. Lett.* **19**, 361.

Du Plessis, J. P. & Masliyah, J. B. 1988 Mathematical modelling of flow through consolidated isotropic porous media. *Transport in Porous Media* **3**, 145–161.

Du Plessis, J. P. & Masliyah, J. B. 1991 Flow through isotropic granular porous media. *Transport in Porous Media* **6**, 207–221.

Edwards, D. A., Shapiro, M., Bar-Yoseph, P. & Shapira, M. 1990 The influence of Reynolds number upon the apparant permeability of spatially periodic arrays of cylinders. *Phys. Fluids* A **2**, 45–55.

Engøy, T., Måløy, K. J., Hansen, A. & Roux, S. 1994 The roughness of two-dimensional cracks in wood. *Phys. Rev. Lett.* **73**, 834.

Firoozabadi, A. & Katz, D. L. 1979 An analysis of high-velocity gas flow through porous media. *J. Petrol. Tech.* February, pp. 211–216.

Forchheimer, P. 1901 Wasserbewegung durch Boden. *Z. Vereines deutscher Ing.* **45** (50), 1782–1788.

Gipouloux, O. 1992 Contribution numérique à l'homogéneisation des équations de Stokes et de Navier-Stokes en milieu poreux. Doctoral Thesis, Université de Bordeaux I; No d'ordre: 673.

Gutfraind, R. & Hansen, A. 1995 Study of fracture permeability using lattice gas automata. *Transport in Porous Media* **18**, 131–149.

Gutfraind, R., Ippolito, I. & Hansen, A. 1995 Study of tracer dispersion in self-affine fractures using lattice gas automata. *Phys. Fluids* **7**, 1938–1948.

Hansen, A., Hinrichsen, E. L. & Roux, S. 1991 Roughness of crack interfaces. *Phys. Rev. Lett.* **66**, 2476.

Hestir, K. & Long, J. C. S. 1990 Analytical expressions for the permeability of random two-dimensional poisson fracture networks based on regular lattice percolation and equivalent porous media theories. *J. Geophys. Res.* **95**, 21565.

Hirata, T. 1989 Fractal dimension of fault systems in Japan: Fractal structure in rock fracture geometry at various scales. *Pure Appl. Geophys.* **121**, 157.

Issa, M. A., Hammad, A. M. & Chudnovsky, A. 1992 Fracture surface characterization of concrete. In *Engineering Mechanics* (ed. L. D. Lutes & J. M. Niedzwecki) ASCE.

Kertész, J., Horvàth, V. & Weber, F. 1993 Self-affine rupture lines in paper sheets. *Fractals* **1**, 67–74.

Lawn, B. 1993 *Fracture of Brittle Solids*, 2nd edn. Cambridge University Press.

Måløy, K. J., Hansen, A., Hinrichsen, E. L. & Roux, S. 1992 Experimental measurements of the roughness of brittle cracks. *Phys. Rev. Lett.* **68**, 213.

Mandelbrot, B. B. 1982 *The Fractal Geometry of Nature*. W. H. Freeman.

Mandelbrot, B. B., Passoja, D. E. & Paullay, A. J. 1984 Fractal character of fracture surfaces of metals. *Nature* **308**, 721.

Mecholsky, J. J., Passoja, D. E. & Feinberg-Ringel, K. 1989 Quantitative analysis of brittle fracture surfaces using fractal geometry. *J. Am. Ceram. Soc.* **72**, 60.

Mei, C. C. & Auriault, J.-L. 1991 The effect of weak inertia on flow through a porous medium. *J. Fluid Mech.* **222**, 647–663.

Milman, V. Y., Blumenfeld, R., Stelmanshenko, N. A. & Ball, R. 1993 Comment on Experimental measurements of the roughness of brittle cracks. *Phys. Rev. Lett.* **71**, 204.

Muskat, M. 1937 *The Flow of Homogeneous Fluids Through Porous Media*. International Human Resources Development Corporation, reprint 1982.

Odling, N. E. 1992 Network properties of a two-dimensional natural fracture pattern. *Pure Appl. Geophys.* **138**, 95.

Peyret, R. & Taylor, D. T. 1983 *Computational Methods for Fluid Flow*. Springer.

Plourabouré, F., Kurowski, P., Hulin, J. P., Roux, S. & Schmittbuhl, J. 1995 Aperture of rough cracks. *Phys. Rev.* E **51**, 1675.

Rasoloarijaona, M. & Auriault, J.-L. 1994 Nonlinear seepage flow through a rigid porous medium. *Eur. J. Mech.* B/*Fluids* **13**, 177–195.

Rottmann, K. 1984 *Matematische Formelsammlung*. Mannheim: Bibliographisches Institut.

Roux, S. 1994 *Fracture Roughness and its Physical Implications*. Lecture Notes in Physics, vol. 437, pp. 235–248. Springer.

Roux, S., Schmittbuhl, J., Vilotte, J.-P. & Hansen, A. 1993 Some properties of self-affine rough surfaces. *Europhys. Lett.* **23**, 277.

Ruth, D. & Ma, H. 1993 Numerical analysis of viscous, incompressible flow in a diverging-converging RUC. *Transport in Porous Media* **13**, 161–177.

Sanchez-Palencia, E. 1980 *Non Homogeneous Media and Vibration Theory*. Lecture notes in Physics, vol. 127. Springer.

Schmittbuhl, J., Sentier, S. & Roux, S. 1993 Field measurements of the roughness of fault surfaces. *Geophys. Res. Lett.* **20**, 639.

Sharon, E., Gross, S. P. & Fineberg, J. 1995 Local crack branching as a mechanism for instability in dynamic fracture. *Phys. Rev. Lett.* **74**, 5097–5099.

Skjetne, E. 1995 High-velocity flow in porous media; analytical, numerical and experimental studies. Doctoral Thesis, Department of Petroleum Engineeering and Applied Geophysics, Norwegian University of Science and Technology.

Snow, D. 1969 Anisotropic permeability of fractured media. *Water Resour. Res.* **5**, 1273.

Souto, H. P. A. 1993 Diffusion-dispersion en milieux poreux: étude numérique du tenseur de dispersion pour quelques arrangements périodiques bidimensionels : "ordonnés" et "désordonnés". Doctoral thesis, Institut National Polytechnique de Lorraine.

Thompson, M. E. 1991 Numerical simulation of solute transport in rough fractures. *J. Geophys. Res.* **96**, 4157.

Tzschichholz, F. & Pfuff, M. 1991 Influence of crack path on crack resistance in brittle materials. In *Fracture Processes in Concrete, Rock and Ceramics* (ed. J. G. M. van Mier, J. G. Rots & A. Bakker), vol. 1. Cambridge University Press.

Velde, B., Dubois, J., Moore, D. & Touchard, G. 1991 Fractal patterns of fractures in granites. *Earth Planet Sci. Lett.* **104**, 25.

Vignes-Adler, M., Le Page, A. & Adler, P. M. 1991 Fractal analysis of fracturing in two African regions, from satelite imaginery to ground scale. *Tectonophysics* **196**, 69.

Voss, R. F. 1985 Random fractal forgeries. In *Fundamental Algorithms for Computer Graphics* (ed. R. A. Earnshaw). NATO ASI Series, vol. F17, pp. 805–835. Springer.

Wodie, J.-C. & Levy, T. 1991 Correction non linéaire de la loi de Darcy. *C. R. Acad. Sci. Paris* II **312**, 157–161.